



Facile synthesis of flower-like $\text{Bi}_{12}\text{O}_{17}\text{Cl}_2/\beta\text{-Bi}_2\text{O}_3$ composites with enhanced visible light photocatalytic performance for the degradation of 4-*tert*-butylphenol

Guangping He, Chunlan Xing, Xin Xiao*, Ruiping Hu, Xiaoxi Zuo, Junmin Nan*

School of Chemistry and Environment, South China Normal University; Guangzhou Key Laboratory of Materials for Energy Conversion and Storage, Guangzhou, 510006, PR China

ARTICLE INFO

Article history:

Received 29 October 2014

Received in revised form 9 January 2015

Accepted 13 January 2015

Available online 15 January 2015

Keywords:

Visible light photocatalysis

$\text{Bi}_{12}\text{O}_{17}\text{Cl}_2/\beta\text{-Bi}_2\text{O}_3$

Heterojunction

4-*Tert*-butylphenol

Photocatalytic mechanism

ABSTRACT

Novel three-dimensional flower-like $\text{Bi}_{12}\text{O}_{17}\text{Cl}_2/\beta\text{-Bi}_2\text{O}_3$ composites are prepared using a facile solvothermal-calcining process and their photocatalytic performances for the degradation of 4-*tert*-butylphenol (PTBP, a representative alkylphenol) are evaluated under visible light irradiation. The formation of such composites is assumed to involve the reduction of Bi(III) to nano-metallic bismuth via a solvothermal process, followed by the reaction of bismuth with oxygen and bismuth oxide chloride hydroxide during the calcination in air. The XRD, XPS, EDS mapping, HRTEM, UV–vis DRS, and photocurrent measurement results indicate that heterojunctions are formed between $\text{Bi}_{12}\text{O}_{17}\text{Cl}_2$ and $\beta\text{-Bi}_2\text{O}_3$ with broad contact interfaces. The as-synthesized $\text{Bi}_{12}\text{O}_{17}\text{Cl}_2/\beta\text{-Bi}_2\text{O}_3$ hybrid materials possess favorable band structures, heterojunction structures, relatively high specific surface areas, and hierarchical micro/nano-structures, resulting in superior photocatalytic and mineralization efficiencies for the decomposition of PTBP under visible light irradiation. The optimum photocatalytic activity of a $\text{Bi}_{12}\text{O}_{17}\text{Cl}_2/\beta\text{-Bi}_2\text{O}_3$ sample is approximately 3, 12, 51, and 107 times higher than the activities of single $\beta\text{-Bi}_2\text{O}_3$, $\text{Bi}_{12}\text{O}_{17}\text{Cl}_2$, nitrogen-doped TiO_2 , and BiOCl, respectively. In addition, the photogenerated reactive species are identified based on free radicals trapping experiments and EPR analysis, which reveals that the photodegradation of PTBP over $\text{Bi}_{12}\text{O}_{17}\text{Cl}_2/\beta\text{-Bi}_2\text{O}_3$ under visible light is dominated by direct hole and superoxide radical oxidation rather than oxidized by hydroxyl radical.

© 2015 Elsevier B.V. All rights reserved.

1. Introduction

Various phenols have been detected in water samples since they are commonly used as reagents or solvents in industrial products or processes. However, this incursion into the water system presents multiple problems [1,2]. For example, most phenols are now recognized as endocrine-disrupting compounds (EDCs), even at very low concentrations [3]. Particularly, these compounds and their metabolites are often not readily biodegradable, resulting in inefficient removal by conventional wastewater treatment plants (WWTPs), which causes increased concern for public health and safety [4]. As a representative alkylphenol, 4-*tert*-butylphenol (PTBP) is widely used to make phosphate esters, fragrances, detergents, oil field chemicals, and demulsifiers. Nevertheless, the treatment of PTBP in wastewaters must be considered

for its estrogenic activity and acute/chronic environmental toxicity [5].

Compared with traditional methods, such as physical adsorption, chemical reactions, and biological degradation, semiconductor photocatalysis has emerged as one of the most innovative technologies for wastewaters treatment. This technology is not only potentially advantageous for the efficient removal and mineralization of phenol contaminants, but also offers an easy way for using energy from natural sunlight or artificial illumination [6]. However, a large number of traditional photocatalysts, such as TiO_2 , ZnO, and SnO_2 , are only active in the ultraviolet light owing to their wide band gaps. In addition, their moderate performances originate from the high recombination rate of photogenerated carriers [7]. The development of novel, visible-light-driven, and highly efficient photocatalysts for the degradation of PTBP remains challenging.

As an important multi-functional material, bismuth oxides have extensive applications in photovoltaic cells, oxygen sensors, nonlinear optical glasses, and as catalysts for selective industrial oxidation processes due to their outstanding properties, including

* Corresponding authors. Tel.: +86 20 39310255; fax: +86 20 39310187.

E-mail addresses: xiaox@scnu.edu.cn (X. Xiao), jmnann@scnu.edu.cn (J. Nan).

their rich polymorphism, adjustable band gaps, high ion conductivity, and so on [8]. In fact, many bismuth-based materials are highly active photocatalysts arising from the intrinsic polarizabilities induced by the Bi 6s² lone pair of electrons, which favors the separation and transfer of photogenerated carriers [9–11]. Of these compounds, Bi₂O₃ is the simplest and most significant bismuth oxides, and it has been suggested that β -Bi₂O₃, the tetragonal polymorph of Bi₂O₃, is one of promising photocatalyst because of its smaller band gap, high oxidation power, and non-toxic properties [12]. Meanwhile, bismuth oxyhalides (BiOX, X=Cl, Br, and I) have also demonstrated excellent photocatalytic reactivities due to their uniquely layered structures [13]. The density functional theory (DFT) calculation has revealed that the valence band maximum of BiOX mainly contains O 2p and X np orbitals, while its conduction band minimum mainly contains the Bi 6p orbital [14]. Inferring the synthesis of bismuth oxyhalides with different Bi:O:X atomic ratios may result in a series of new photocatalysts with various band structure features [15]. For example, while BiOCl is only active in UV light ($E_g \sim 3.5$ eV), Bi₂₄O₃₁Cl₁₀ [16], Bi₃O₄Cl [17], and Bi₁₂O₁₇Cl₂ [18] have reported visible light photocatalytic activities for the decomposition of organic compounds. Nevertheless, owing to restricted crystal growth under routine conditions, the synthesis of nanostructured bismuth oxyhalides with different Bi:O:X ratios is not an easy job [19].

Furthermore, to improve the catalytic activity of photocatalysts, one popular and effective strategy is to construct heterojunctions by coupling two or more semiconductors with well-matched band structures. Such a heterogeneous system allows a photocatalyst to use more visible light and effectively to separate the photogenerated hole-electron pairs [20]. To date, many Bi₂O₃- or BiOX-based hybrid materials, such as Bi₂O₃/TiO₂ [21], Bi₂O₃/BiVO₄ [22], Bi₂O₃/Bi₂WO₆ [23], Bi₂O₃/Bi₂MoO₆ [24], Bi₂O₃/NiFe₂O₄ [25], Bi₂O₃/Bi₂O_{4-x} [26], BiOCl/Fe₃O₄ [27], BiOBr/C₃N₄ [28], BiOI/TiO₂ [29], and BiOI/BiOCl [30], have been synthesized and demonstrated enhanced visible light photocatalytic reactivities. The main challenge of constructing a high-activity heterojunction photocatalyst system is finding two semiconductors with well-matched band structures as well as can effectively contact each other. Previously, reports regarding the synthesis and photocatalytic properties of Bi₂O₃/BiOX heterojunctions were very limited [31,32]. Particularly, the fabrication of nano Bi₂O₃/O-rich BiOX [15] heterojunctions has not been explored.

Motivated by the above considerations, herein we present a solvothermal-calcining route for synthesizing Bi₁₂O₁₇Cl₂/ β -Bi₂O₃ nano-heterojunctions with flower-like micro/nano architectures. Photocatalytic experiments displayed that the as-synthesized Bi₁₂O₁₇Cl₂/ β -Bi₂O₃ composites exhibit excellent photocatalytic activities for degrading PTBP under visible light illumination, which are much better than those of individual β -Bi₂O₃, Bi₁₂O₁₇Cl₂, nitrogen-doped TiO₂ (N-TiO₂), or BiOCl. In addition, the possible photocatalytic mechanisms of the system were discussed.

2. Experimental

2.1. Materials and methods

The PTBP was obtained from Aladdin Reagent Co., Ltd. The bismuth nitrate pentahydrate (Bi(NO₃)₃·5H₂O) and potassium chloride (KCl) were purchased from Tianjin Kermel Chemical Reagent Co., Ltd. and the ethylene glycol (EG) was purchased from Chinasun Specialty Products Co., Ltd. All of the chemicals were analytical grade and used as received.

In a typical synthesis procedure, 1.5 mmol of Bi(NO₃)₃·5H₂O and 1.5 mmol of D-fructose were completely dissolved in 35 mL EG to obtain solution A. In addition, a specified amount of KCl was

dissolved in EG to obtain solution B. Then, solution B was added dropwise to solution A with constantly stirring. The mixture was poured into a Teflon-lined stainless-steel autoclave and incubated in an oven at 160 °C for 15 h. After completing the reaction, the precipitates were segregated by centrifugation, washed several times with distilled water and absolute ethanol, and dried in an oven at 60 °C. Finally, the products were calcined in air at 300 °C for 1 h. Samples synthesized with Bi:Cl at atomic ratios of 1:0, 20:1, 10:1, 8:1, 7:1, and 6:1 were denoted as S1, S2, S3, S4, S5, and S6, respectively. A sample synthesized using a Bi:Cl atomic ratio of 6:1 and calcined at 500 °C for 1 h was labeled as S7.

For comparison, a pure BiOCl sample was obtained using the same process with a Bi:Cl atomic ratio of 1:1. In addition, a N-TiO₂ sample (Fig. S1, Supporting information) was prepared by a solvothermal method using ethylenediamine as the nitrogen source, as described by Yang et al. [33].

2.2. Catalyst characterization

The crystalline structures and compositions of samples were determined by powder X-ray diffraction (XRD) using a Bruker D8 Advance X-ray diffractometer (Bruker AXS, Germany) with Cu K α radiation. X-ray photoelectron spectroscopy (XPS, Thermo Scientific ESCALAB 250Xi, USA) equipped with an Al K α source was used to investigate the surface properties. The morphologies of samples were observed by a field-emission scanning electron microscope (FE-SEM, Zeiss Ultra 55, Germany). Chemical mapping was achieved by combining the scanning module of the microscope to the energy dispersive X-ray spectroscopy (EDS) detector. Microstructures and phase interfaces were revealed by using a field emission transmission electron microscopy (TEM, Tecnai G2 F20, FEI). The specific surface areas were measured using nitrogen adsorption-desorption isotherms at 77 K, according to the Brunauer-Emmett-Teller analysis (BET, ASAP 2020, Micromeritics, USA). A desorption isotherm was used to determine the pore size distribution using the Barrett-Joyner-Halenda (BJH) method. The UV-vis diffuse reflection spectra (DRS) were measured on a UV-vis spectrophotometer (UV-3010, Hitachi, Japan) with BaSO₄ as a reference and were converted from reflection to absorbance by using the Kubelka-Munk method. The Mott-Schottky experiments were conducted to evaluate the band structure of as-synthesized samples with an electrochemistry workstation (Princeton PARSTAT 2273, USA) using a working electrode (an appropriate amount of the sample suspension on a conductive indium tin oxide glass), a platinum plate as counter electrode, and a standard saturated calomel electrode (SCE) as reference electrode. A 0.5 mol L⁻¹ Na₂SO₄ aqueous solution was used as the electrolyte. The potential range was -0.8 to +0.4 V at a constant frequency of 1000 Hz. Photocurrent measurements were carried out using a CHI 660 C electrochemical station (Chenhua Instruments Co. Shanghai, China) in a standard three-electrode configuration with the as-prepared samples as the working electrodes, a platinum plate as the counter electrode, and a commercial Ag/AgCl electrode as the reference electrode. A 0.5 mol L⁻¹ Na₂SO₄ aqueous solution was used as the electrolyte. A 300 W xenon lamp (PLS-SXE300/300UV) assembled with a UV light cut off filter ($\lambda > 420$ nm) was used as the visible light irradiation source. Electron paramagnetic resonance (EPR) spectra were recorded at room temperature using a JES FA-200 spectrometer (JEOL, Japan) equipped with a 500 W Xe lamp and a cut-off filter ($\lambda > 420$ nm), and 5,5-dimethyl-1-pyrroline-N-oxide (DMPO) was used as a spin trap.

2.3. Photocatalytic activity measurements

Photocatalytic degradation experiments were performed in a photochemical reactor (XPA-VII, Nanjing Xujiang Machine-

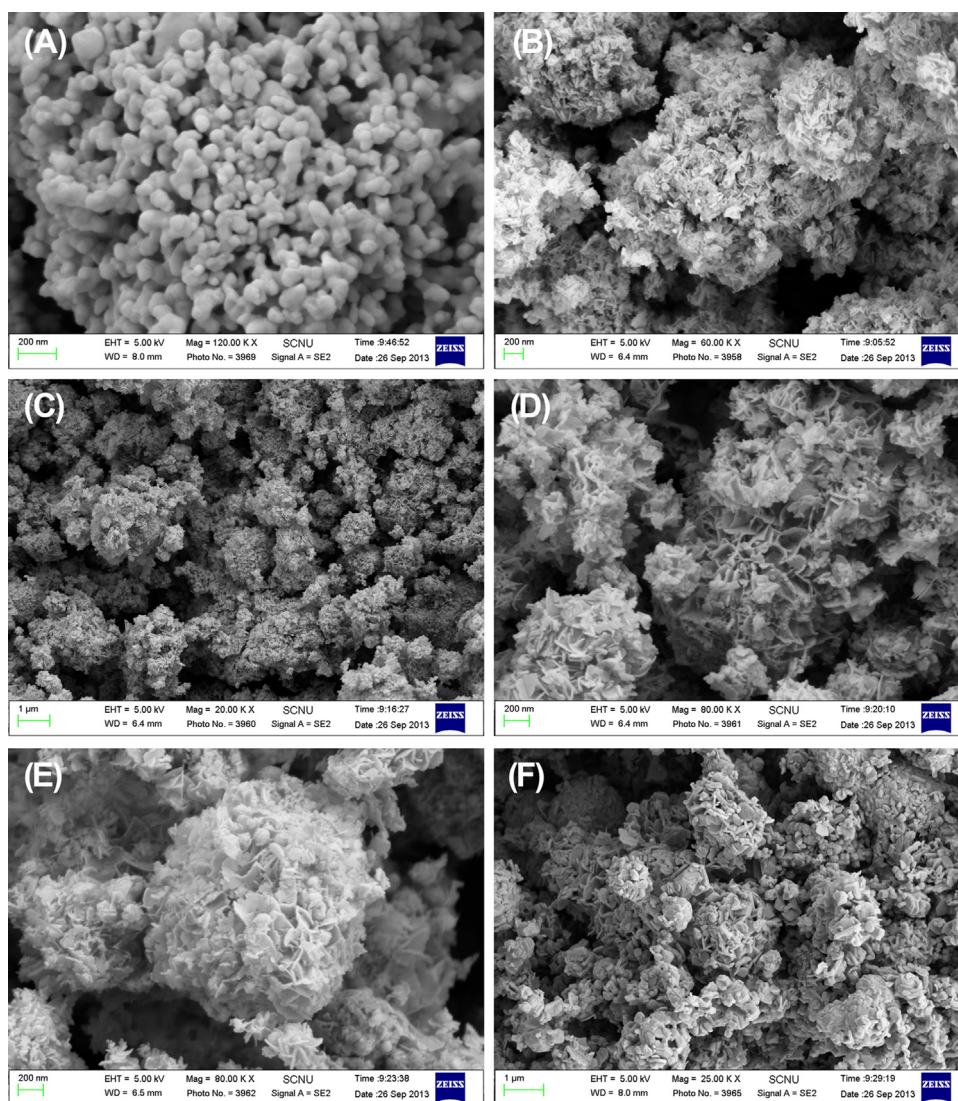


Fig. 1. SEM images of the as-synthesized samples: (A) S1, (B) S3, (C, D) S4, (E) S6, and (F) S7.

electronic Plant, China) equipped with a 1000 W Xe lamp and a 420 nm cutoff filter as the light source. In each experiment, a certain amount of the as-synthesized catalyst (varying from 0.5 to 2.5 g L⁻¹, typically 1 g L⁻¹) was added to a 50 mL reaction solution containing PTBP with various initial concentrations (ranging from 20 to 100 mg L⁻¹, typically 60 mg L⁻¹). Before irradiation, the solution containing the catalyst was stirred for 1 h in the dark to let the system to reach adsorption equilibrium. During the photocatalytic process, about 3 mL of the suspension was taken out at a specified time. Subsequently, the solids were removed from the solution using a 0.45-μm nitrocellulose filter, and the filtrate was scanned using a UV–vis spectroscopy (UV-1800, Shimadzu, Japan, λ_{max} = 274 nm) to measure the PTBP concentrations. The total organic carbon (TOC) content was determined using an automatic total organic carbon analyzer (TOC-V, Shimadzu, Japan).

3. Results and discussion

3.1. Catalyst characterization

The morphology and structure of the as-synthesized samples were investigated by SEM. As presented in Fig. 1A, the sample S1 (without addition of Cl⁻) consists of a large number of nanospheres

with average diameters of ~80 nm, which is in agreement with our previous report [34]. However, after the addition of Cl⁻ to the system, the as-synthesized S3, S4, and S6 samples (Figs. 1B–E) appear to flower-like micro/nano structures that are composed of numerous nanoflakes with thicknesses of ~20 nm and measurements of ~200 nm in the other two dimensions. These structures are significantly different from those observed in sample S1. In addition, even after calcination at a higher temperature (500 °C, sample S7, Fig. 1F), this flower-like morphology is still maintained. However, the thickness of the nanoflakes increases and the other two dimensions decrease.

Figs. 2A and S2–S8 (Supporting information, each sample separately) show the XRD patterns of the as-synthesized samples. All of the peaks of sample S1 can be reliably indexed as β-Bi₂O₃ (tetragonal, JCPDS No. 78-1793), while sample S7 (Bi:Cl = 6:1, calcined at 500 °C) can be unambiguously recognized as pure tetragonal-phase Bi₁₂O₁₇Cl₂ (JCPDS No. 37-0702). Then the samples S2–S5 can be identified as mixed phase of Bi₁₂O₁₇Cl₂ and β-Bi₂O₃, and the Bi₁₂O₁₇Cl₂ contents in the composites increased as the amount of added chloride ions increased (from S2 to S5). Composition quantitative analysis of multi-phase samples was established using the RIR (relative intensity ratios) method [35,36]. The RIR values for a phase was defined as the intensity ratio of its strongest peak to that of corundum (α-Al₂O₃) in a 50:50 mixture by weight. When sam-

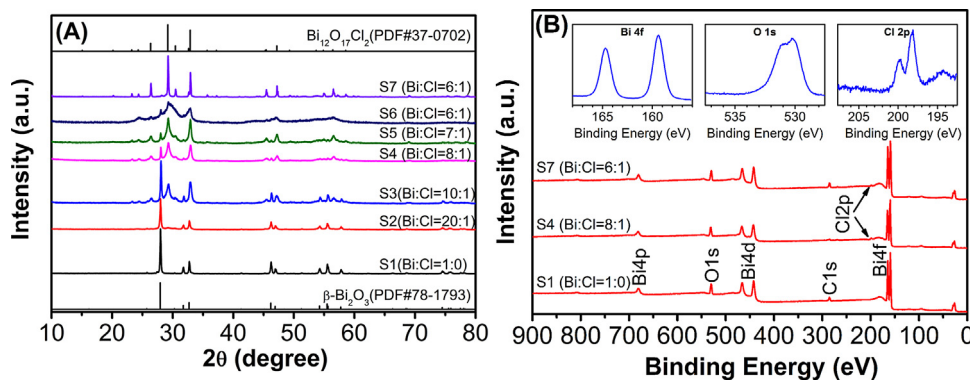


Fig. 2. (A) XRD patterns of samples S1–S7. (B) XPS spectra of samples S1, S4, and S7; the insets illustrate the high-resolution XPS spectra of sample S4 (Bi 4f, O 1s, and Cl 2p).

Table 1
Quantitative analysis and crystalline sizes of the as-synthesized samples.

Samples	Weight ratio (wt%)		Crystalline size (nm)	
	Bi ₁₂ O ₁₇ Cl ₂	β-Bi ₂ O ₃	Bi ₁₂ O ₁₇ Cl ₂	β-Bi ₂ O ₃
S1	0	100		63.9
S2	10.93	89.07	22.0	58.5
S3	53.63	46.37	20.6	55.0
S4	76.86	23.14	19.5	72.9
S5	88.21	11.79	19.8	50.6
S7	100	0	>100	

ples are consisted of two phases, the weight ratio of each phase can be calculated using the following formula:

$$W_a = \frac{I_a}{I_a + (I_b / (RIR_b / RIR_a))} \quad (1)$$

$$W_b = \frac{I_b}{I_b + (I_a / (RIR_a / RIR_b))} \quad (2)$$

where W_a and W_b are the weight ratios of phase a and b, respectively; RIR_a and RIR_b are the RIR values of phase a and b, respectively; I_a and I_b are integrated intensities of the strongest peak of phase a and b, respectively; for Bi₁₂O₁₇Cl₂ and β-Bi₂O₃, I values determined from Bi₁₂O₁₇Cl₂ (1 1 7) plane and β-Bi₂O₃ (2 0 1) plane, respectively. The calculated weight ratios of as-prepared samples are listed in Table 1. The results of evaluation are very close to the feed ratio in the synthesis. In addition, the average crystalline sizes of the as-prepared samples are calculated according to the Scherrer formula [37] and are also summarized in Table 1. The results are in agreement with above SEM observations. What's more, the XPS spectra of as-synthesized samples (Fig. 2B) further reveal that samples S4 and S7 contain small amounts of Cl, whereas sample S1 consists of pure bismuth oxide. Figs. 2B and S9 (Supporting information) reveal the high-resolution XPS spectra of Bi 4f, O 1s, and Cl 2p for the S4 sample (Bi:Cl = 8:1). The two strong peaks in the Bi region of 159.3 and 164.6 eV are respectively assigned to Bi 4f 7/2 and Bi 4f 5/2, which are characteristic of Bi³⁺ [38,39]. The O 1s core level spectrum can fit the two peaks well, and the dominant peak at 530.0 eV is characteristic of a bismuth-oxygen bond, while the other peak at 531.2 eV is attributed to chemisorbed H₂O or OH[−] on the surface [39,40]. Similarly, the Cl 2p spectrum presences a well doublet peaks at 199.8 and 198.2 eV, which can be ascribed to Cl 2p 1/2 and Cl 2p 3/2, respectively [38,41]. In previous report [42], some authors found that reduced Bi oxide phases or zerovalent Bi may also presence in Bi-based catalysts. However, under current condition, it did not find a Bi peak below 157.0 eV in sample S4 (Fig. S9A, Supporting information). And through carefully analysis, the unusual shoulder peak at 194.4 eV in Cl 2p can be interpreted as a small amount of impure derive from its precursor

(Fig. S9B, Supporting information). Therefore, Bi₁₂O₁₇Cl₂/β-Bi₂O₃ composites can be readily synthesized by using this solvothermal-calcining route, and the ratios of Bi₁₂O₁₇Cl₂ and β-Bi₂O₃ are easily controlled between the composites by adding a low concentration of Cl[−].

Unexpectedly, sample S6 (Bi:Cl = 6:1, calcined at 300 °C) revealed a mixture of Bi₁₂O₁₇Cl₂, β-Bi₂O₃, and Bi₃O₄Cl (JCPDS No. 36-0760) instead of the expected pure Bi₁₂O₁₇Cl₂. To further investigate the effects of the amount of chloride ions on the composition of products, a series of supplementary experiments were conducted with increasing chloride ion contents. As presented in Fig. S10 (Supporting information), the samples with initial Bi:Cl atomic ratios of 5:1 and 4:1 can be identified as the mixed phases of Bi₁₂O₁₇Cl₂ and Bi₃O₄Cl. The sample with an initial atomic ratio of Bi:Cl = 3:1 can be identified as the mixed phase of Bi₃O₄Cl and Bi₄O₅Cl₂ (JCPDS No. 41-0658), the sample with an initial atomic ratio of Bi:Cl = 2:1 can be recognized as the mixed phase of Bi₃O₄Cl, Bi₄O₅Cl₂ and BiOCl (JCPDS No. 82-0485), and the sample with an initial atomic ratio of Bi:Cl = 1:1 can be identified as pure BiOCl. The results suggest that, except for BiOCl, other single-phase bismuth oxychlorides are not easily obtained under the current conditions (calcined at 300 °C), and that the compositions of the products are significantly influenced by the amount of chloride ions added and the temperature of the heat treatment. Therefore, a subsequent study should focus on the addition of a small amount of chloride ions (Cl:Bi < 6), i.e., the mixed phase of Bi₁₂O₁₇Cl₂ and β-Bi₂O₃ samples. The reason for the formation of Bi₁₂O₁₇Cl₂ instead of other bismuth oxychlorides or their mixtures in low Cl[−] concentration is not clear now and needs further investigation. It is likely to be associated with bismuth is obviously in excess in the system and Bi₁₂O₁₇Cl₂ has smaller formation enthalpy among bismuth oxychlorides [43]. This assumption may be further confirmed in another study on synthesis of bismuth oxychlorides using Bi₂O₃ and BiOCl as starting materials, which found that pure Bi₁₂O₁₇Cl₂ can be obtained at a relatively lower temperature (350–400 °C) than other bismuth oxychlorides [44]. In addition, according to XRD and XPS analyses, it is hard to detect that any Cl was doped into β-Bi₂O₃ matrix, which may be attributed to the lower calcination temperature.

To elucidate the possible formation process of the Bi₁₂O₁₇Cl₂/β-Bi₂O₃ composites, the precursors (before calcination) were analyzed by XRD and SEM. As shown in Fig. 3A, in the absence of Cl[−], the characteristic diffraction peaks of the precursor represent metallic bismuth (JCPDS No. 85-1329), while the obtained product with an initial atomic ratio of Bi:Cl = 1:1 is BiOCl. The formation of the bismuth precursor and β-Bi₂O₃ (sample S1) can be explained by “in situ reduction” following “in situ oxidation” mechanism, as described in our previous report [34]. In this case, the zerovalent bismuth nanospheres were formed by the solvothermal reduction and then converted to β-Bi₂O₃ after calcination in an air atmo-

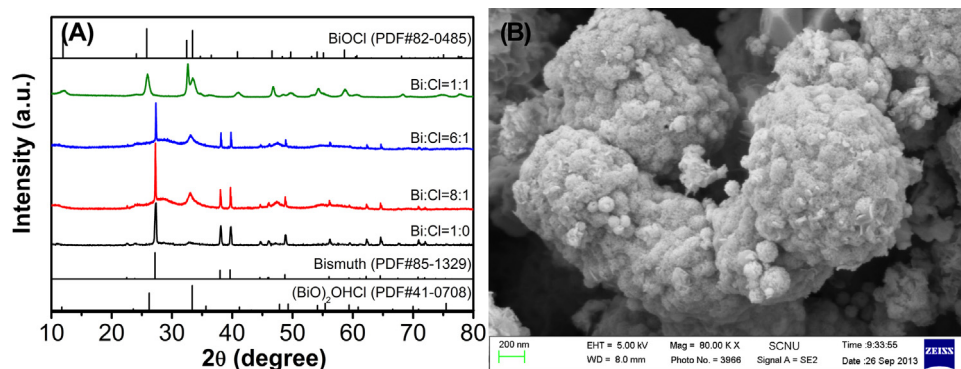


Fig. 3. (A) XRD patterns of the samples before calcination using different Bi:Cl atomic ratios. (B) SEM images of sample S4 before calcination.

sphere. Thanks to its higher thermal stability, the BiOCl precursor is stable with enhanced crystallinity after it is calcined at 300 °C (Fig. S10, Supporting information). However, when Cl^- is added, the precursors can be identified as the mixed phase of metallic bismuth and bismuth oxide chloride hydroxide $((\text{BiO})_2\text{OHCl})$ (JCPDS No. 41-0708). As a tetragonal phase structure, $((\text{BiO})_2\text{OHCl})$ can easily grow into sheet-like structures owing to its intrinsic crystalline nature, which tends to further aggregate into larger particles by EG-mediation to decrease its surface energy [45] (Fig. 3B). Next, the metallic bismuth was oxidized by oxygen and reacted with bismuth oxide chloride hydroxide to form $\text{Bi}_{12}\text{O}_{17}\text{Cl}_2/\beta\text{-Bi}_2\text{O}_3$ composites during the calcination process. Simultaneously, the morphology of the samples further developed into flower-like micro/nano structures (Fig. 1).

To further understand the relationships between $\text{Bi}_{12}\text{O}_{17}\text{Cl}_2$ and $\beta\text{-Bi}_2\text{O}_3$ in the composites, SEM, EDS, EDS mapping, TEM, and high-resolution TEM (HRTEM) analyses were performed. As presented in Figs. 4A and B, the EDS shown that the S4 sample contained Bi, O, and Cl with an atomic Bi:Cl ratio of 6.5:1, which is close to the the-

oretical ratio of 8:1. Besides, the EDS mapping clearly revealed that Bi, O, and Cl are uniformly distributed on the surface of the sample. The TEM image (Fig. 4C) reveals that the sample has a diameter of 1–2 μm with a flower-like appearance that consists of numerous nanosheets, which is agrees with the SEM images. And the HRTEM image (Fig. 4D) confirms that there are two lattice sets with d spacings of 0.27 and 0.32 nm, which correspond to the (200) plane of $\text{Bi}_{12}\text{O}_{17}\text{Cl}_2$ and the (201) plane of $\beta\text{-Bi}_2\text{O}_3$, respectively. The results indicate that heterojunctions were constructed between $\beta\text{-Bi}_2\text{O}_3$ and $\text{Bi}_{12}\text{O}_{17}\text{Cl}_2$ in the sample S4 with broad interaction interfaces.

Fig. 5 displays the UV–vis DRS of the as-synthesized samples S1 ($\beta\text{-Bi}_2\text{O}_3$), S4 ($\text{Bi}_{12}\text{O}_{17}\text{Cl}_2/\beta\text{-Bi}_2\text{O}_3$), and S7 ($\text{Bi}_{12}\text{O}_{17}\text{Cl}_2$). The maximal absorbance wavelengths of S1, S4, and S7 were approximately 544, 539, and 512 nm, respectively, suggesting their ability to absorb visible light. Correspondingly, the materials show significantly different in colors, ranging from dark yellow to light yellow (inset of Fig. 5). Next, the band gap energies of these samples were calculated using the following equation [15]:

$$\alpha(h\nu) = A(h\nu - E_g)^{n/2} \quad (3)$$

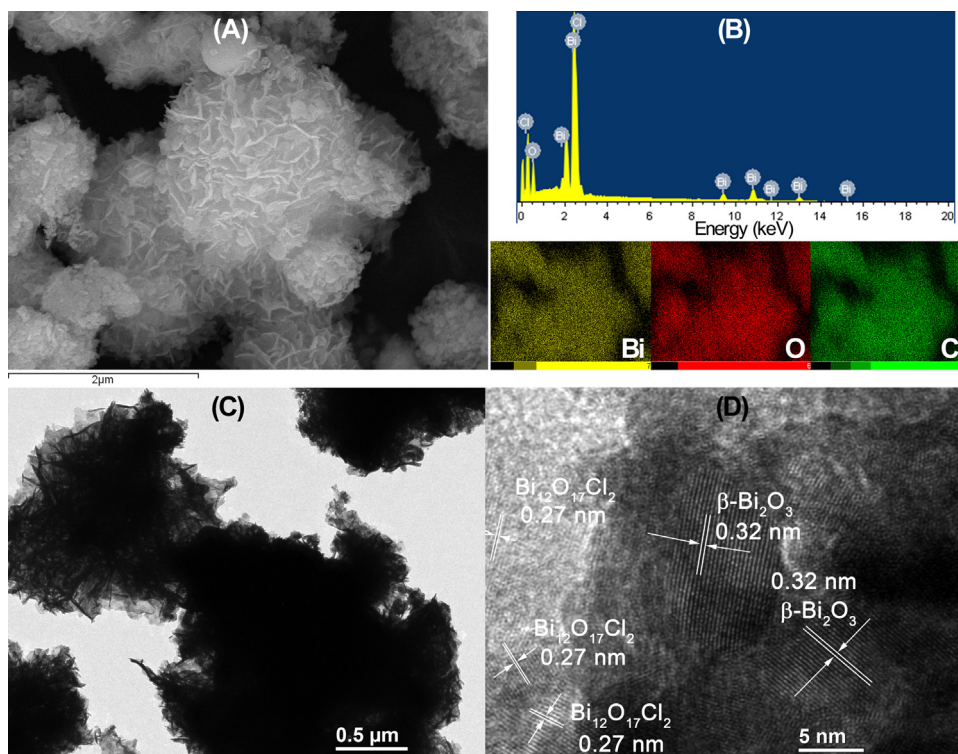


Fig. 4. (A) SEM image; (B) EDS spectrum and mapping distribution of Bi, O, and Cl; (C) TEM image; and (D) high-resolution TEM image of the sample S4.

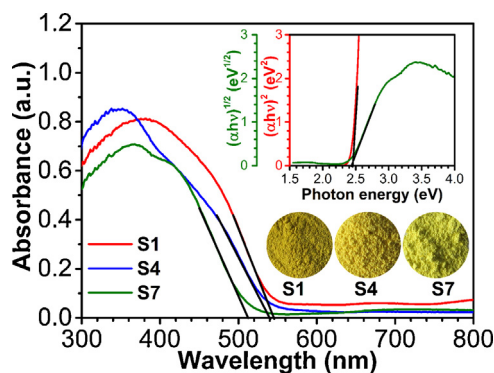


Fig. 5. UV-vis diffuse reflection spectra of samples S1, S4, and S7; the inset displays a plot of $(\alpha h\nu)^{1/2}$ vs. photon energy ($h\nu$) and the optical images of the corresponding samples. (For interpretation of the references to colour in the text, the reader is referred to the web version of this article.)

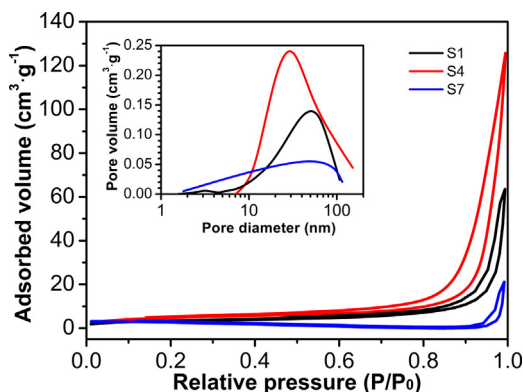


Fig. 6. Nitrogen adsorption-desorption isotherms and the corresponding pore size distribution curve (inset) for the as-synthesized samples S1, S4, and S7.

where α , ν , E_g and A are the absorption coefficient, light frequency, band gap energy, and a constant, respectively, and n is 4 for the indirect transition of $\text{Bi}_{12}\text{O}_{17}\text{Cl}_2$ [18] whereas it is 1 for the direct transition of $\beta\text{-Bi}_2\text{O}_3$ [46]. Then, the band gap energy of $\beta\text{-Bi}_2\text{O}_3$ (S1) and $\text{Bi}_{12}\text{O}_{17}\text{Cl}_2$ (S7) were estimated to be 2.45 and 2.43 eV (inset of Fig. 5), respectively. The E_g values of $\beta\text{-Bi}_2\text{O}_3$ and $\text{Bi}_{12}\text{O}_{17}\text{Cl}_2$ determined in this study are close to those reported in the literatures [18,47].

Fig. 6 demonstrates the nitrogen adsorption-desorption isotherms for samples S1 ($\beta\text{-Bi}_2\text{O}_3$), S4 ($\text{Bi}_{12}\text{O}_{17}\text{Cl}_2/\beta\text{-Bi}_2\text{O}_3$), and S7 ($\text{Bi}_{12}\text{O}_{17}\text{Cl}_2$). All isotherms are recognized as type IV with H3 hysteresis loop, which implies that the samples have mesoporous structures [48]. The BET surface areas of the samples were esti-

mated using N_2 isotherms to be 11.8, 18.0, and $2.34 \text{ m}^2 \text{ g}^{-1}$ for samples S1, S4, and S7, respectively. The results indicate that the specific surface area of $\text{Bi}_{12}\text{O}_{17}\text{Cl}_2/\beta\text{-Bi}_2\text{O}_3$ is 1.5 and 7.5 times larger than that of pure $\beta\text{-Bi}_2\text{O}_3$ and $\text{Bi}_{12}\text{O}_{17}\text{Cl}_2$, respectively, which can be attributed to its three-dimensional flower-like structures. The lowest specific surface area of sample S7 may be ascribed to its larger particle size after calcination at a higher temperature (500°C). Then, the corresponding pore size distributions of the samples were calculated using the BJH method (also inset in Fig. 6), which revealed that the mesoporous average diameters were 12.2, 9.66, and 5.57 nm for samples S1, S4, and S7, respectively, and that these pores were broadly distributed. The mesoporous feature with broadly distributed pores may result from the inter-nanoflake/nanosheet spaces within the as-prepared samples.

3.2. Photocatalyst activity

Photocatalytic degradation of PTBP over the as-synthesized samples was evaluated under visible light irradiation and compared with the direct photolysis (Blank), N-TiO_2 , and pure BiOCl , as shown in Fig. 7A. It is clearly revealed that the PTBP was hardly diminished after direct light irradiation. Under identical reaction for 90 min, only 2.3% and 6.7% degradation occurred relative to the BiOCl and N-TiO_2 , respectively, while the single $\text{Bi}_{12}\text{O}_{17}\text{Cl}_2$ (sample S7) and $\beta\text{-Bi}_2\text{O}_3$ (sample S1) achieved degradation efficiencies of 24.2% and 68.4%, respectively. However, all of the synthesized composites (sample S2–S6) exhibited enhanced photocatalytic activities, and a 97.0% removal ratio was obtained for sample S4, indicating its excellent visible light photocatalytic performance. The degradation kinetics of PTBP were examined by fitting the experimental data to the following pseudo first-order kinetics equation [49]:

$$-\ln\left(\frac{C_t}{C_0}\right) = k_{\text{app}}t \quad (4)$$

where C_0 and C_t are the reactant concentrations at $t=0$ and t , respectively, and k_{app} (min^{-1}) is the apparent reaction rate constant. The results (Fig. 7B) show that the k_{app} values for BiOCl , N-TiO_2 , and S1–S7 samples were 0.035, 0.075, 1.329, 1.588, 2.777, 3.807, 2.481, 2.256, 1.214, and $0.319 \times 10^{-2} \text{ min}^{-1}$, respectively. Namely, the as-synthesized sample S4 ($\text{Bi:Cl}=8:1$) exhibited an photocatalytic activity that was approximately 3, 12, 51, and 107 times higher than the single $\beta\text{-Bi}_2\text{O}_3$, $\text{Bi}_{12}\text{O}_{17}\text{Cl}_2$, N-TiO_2 , and BiOCl , respectively. To test the stability and reusability of the as-synthesized composites, the catalyst (sample S4) was reused for three times under the same conditions, and compared with the single $\beta\text{-Bi}_2\text{O}_3$ and a commercially available $\beta\text{-Bi}_2\text{O}_3$ sub-microspheres, as displayed in Fig. S11 (Supporting information). The results reveal that the recyclability of $\beta\text{-Bi}_2\text{O}_3$ samples are very poor, which may be ascribed to its structural instability in

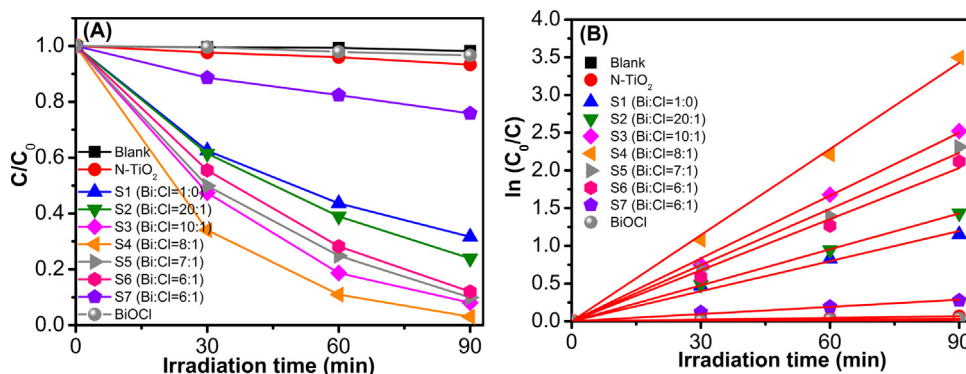


Fig. 7. (A) Photocatalytic degradation kinetics of PTBP with an initial concentration of 60 mg L^{-1} and with 1 g L^{-1} catalyst on the blank (without catalyst), and as-synthesized samples of S1–S7, BiOCl , and N-TiO_2 under visible light irradiation; (B) linear plots of $\ln(C_0/C_t)$ versus time.

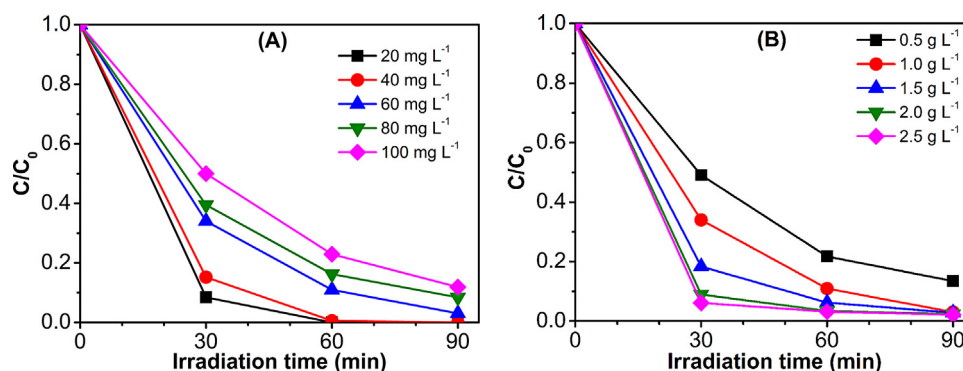


Fig. 8. Effects of (A) the initial concentration of PTBP and (B) the catalyst dose on the photocatalytic performance of Bi₁₂O₁₇Cl₂/β-Bi₂O₃ (sample S4). Experimental conditions: the catalyst dose is 1 g L⁻¹ for the PTBP concentration experiments, while $C_0 = 60$ mg L⁻¹ for the experiments using a varied catalyst dose.

photocatalytic reaction [50], while the Bi₁₂O₁₇Cl₂/β-Bi₂O₃ sample demonstration a relatively good stability during three cycles, which is important for its practical application.

Various initial PTBP concentrations in solution (ranging from 20 to 100 mg L⁻¹) and a series photocatalyst doses (sample S4, from 0.5 to 2.5 g L⁻¹) were used to investigate the effects of the operating conditions on the system. It can be observed that from Fig. 8A, the lower PTBP concentrations were treated more efficiently. This result potentially occurred because additional organic may adsorb onto the catalysts surface as the concentration of PTBP rises, reducing the photo-generation of the reactive oxygen species as the active sites are overloaded. Meanwhile, the degradation efficiency of PTBP improved when the photocatalyst concentration increased (Fig. 8B), yet the enhancement was not notable when the concentration of catalyst exceeded 1.5 g L⁻¹. Obviously, lower catalytic performance occurred when fewer catalyst was used since less active catalytic sites were available. However, if the dosage is too high, caused by the aggregation of catalyst particles, the opacity and light scattering of the system increase, and the number of catalytic surface active sites decreases [51]. Thus, the degradation efficiency of the PTBP will no longer increase.

It is very important of the effective mineralization of organic compounds to avoid secondary pollution in the practical application of photocatalytic technology. In this system, total organic carbon (TOC) was chosen as a mineralization index, and the time independence of the TOC data in the PTBP solution during the photocatalytic process are presented in Fig. 9. It is clearly shown that the TOC declines with irradiation time. After irradiation for 120 min, 94.3% of the TOC was eliminated, demonstrating that the PTBP was effectively mineralized by the as-synthesized Bi₁₂O₁₇Cl₂/β-Bi₂O₃ composites under visible light irradiation.

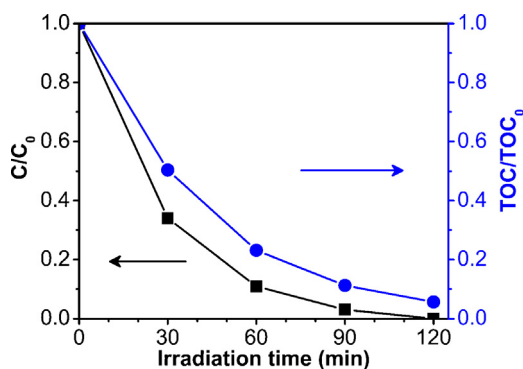


Fig. 9. Comparison of the photocatalytic degradation and TOC removal efficiency using the as-synthesized Bi₁₂O₁₇Cl₂/β-Bi₂O₃ (sample S4) with an initial PTBP concentration of 60 mg L⁻¹ and a catalyst concentration of 1 g L⁻¹ under visible light irradiation.

3.3. Mechanism

The high photocatalytic performance of the as-synthesized Bi₁₂O₁₇Cl₂/β-Bi₂O₃ composites may be related to their unique energy bands and nanostructures. It is generally believed that the activity of a photocatalyst depends on its charge carrier generation and separation. In addition, coupled semiconductors with different conduction band (CB) and valence band (VB) redox energy levels can enhance the efficiency of interfacial charge transfer [52]. Mott-Schottky experiments were conducted to estimate the band positions of the as-synthesized β-Bi₂O₃ (sample S1) and Bi₁₂O₁₇Cl₂ (sample S7). As shown in Fig. 10A, the flat-band potentials of Bi₁₂O₁₇Cl₂ and β-Bi₂O₃ are evaluated to be -0.42 V and -0.25 V vs. SCE (-0.18 and -0.01 V vs. NHE), respectively, which is consistent with the previous investigations [18,53]. The results indicate that the conduction band bottom potential (E_{CB}) of Bi₁₂O₁₇Cl₂ is more negative than that of β-Bi₂O₃, while the valence band top potential (E_{VB} , obtained using the equation: $E_{VB} = E_{CB} + E_g$) of Bi₁₂O₁₇Cl₂ is more positive than that of β-Bi₂O₃. Based on the flat-band potentials levels of these two semiconductors, a band structure illustration for the Bi₁₂O₁₇Cl₂/β-Bi₂O₃ composites is drawn. As presented in Fig. 10B, once the Bi₁₂O₁₇Cl₂ and β-Bi₂O₃ are electronically coupled together, the band alignment between the two kinds of semiconductors results in the development of a heterojunction with a well-matched band structure. Upon visible light irradiation, the photogenerated electrons are generally transferred from Bi₁₂O₁₇Cl₂ to β-Bi₂O₃ due to the CB offset of 0.17 eV, whereas the photogenerated holes transferred from β-Bi₂O₃ to Bi₁₂O₁₇Cl₂ are driven by a VB offset of 0.19 eV, leading to more effective separation of holes and electrons consequently contributing to the enhanced photocatalytic performances.

To further confirm and gain insight regarding the higher separation efficiency of photo-induced charges in the Bi₁₂O₁₇Cl₂/β-Bi₂O₃ hybrid materials, the photocurrents were also measured for the β-Bi₂O₃ (sample S1), Bi₁₂O₁₇Cl₂/β-Bi₂O₃ (sample S4), and Bi₁₂O₁₇Cl₂ (sample S7) electrodes, as shown in Fig. 10C. It can be seen that fast photocurrent responses via on-off cycles appeared in these electrodes under visible light irradiation, which could be directly related with the separation efficiency of the photogenerated carriers. The photocurrent of the Bi₁₂O₁₇Cl₂/β-Bi₂O₃ heterojunction electrodes is significantly higher than that of the single Bi₁₂O₁₇Cl₂ or β-Bi₂O₃, indicating that the heterojunction is more effective to separate the electron-hole pairs [54]. Therefore, the construction of Bi₁₂O₁₇Cl₂/β-Bi₂O₃ heterojunctions largely reduced the recombination rate of the photogenerated electrons and holes, resulting in higher photodegradation activity.

In addition to the intrinsic heterojunction, the as-synthesized Bi₁₂O₁₇Cl₂/β-Bi₂O₃ composites own higher specific surface areas

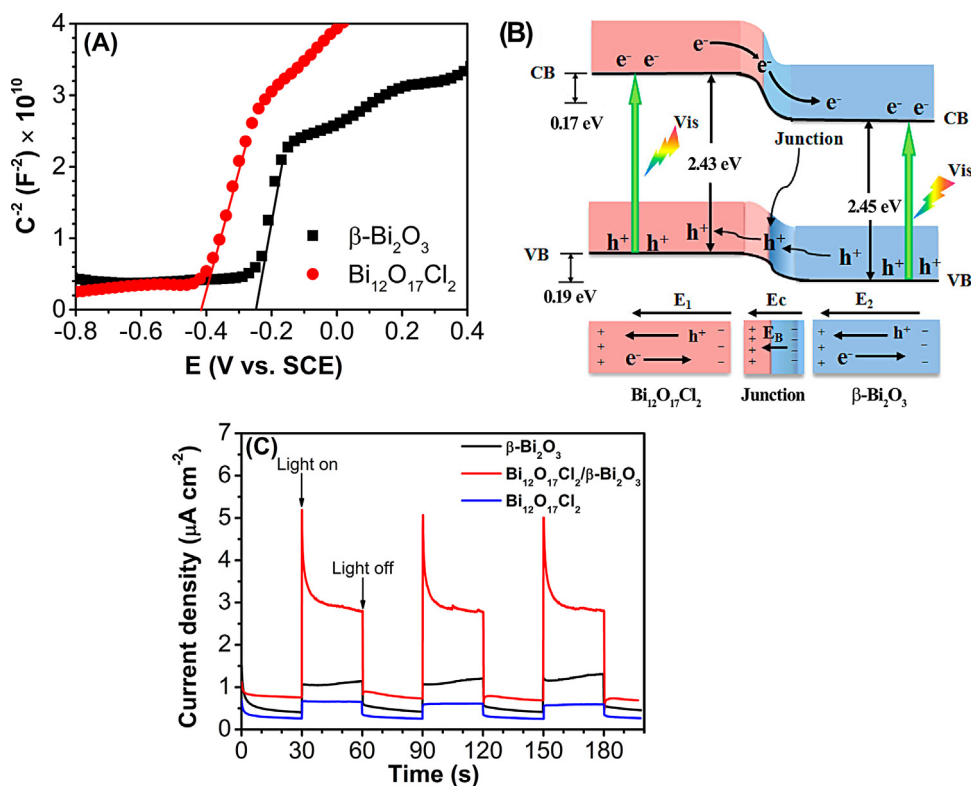


Fig. 10. (A) Mott-Schottky plots for the as-synthesized $\beta\text{-Bi}_2\text{O}_3$ (S1) and $\text{Bi}_{12}\text{O}_{17}\text{Cl}_2$ (S7). (B) Schematic illustration of electron-hole separation and transport at the $\text{Bi}_{12}\text{O}_{17}\text{Cl}_2/\beta\text{-Bi}_2\text{O}_3$ heterojunction interface. (C) Photocurrent transient responses for $\beta\text{-Bi}_2\text{O}_3$ (S1), $\text{Bi}_{12}\text{O}_{17}\text{Cl}_2/\beta\text{-Bi}_2\text{O}_3$ (S4), and $\text{Bi}_{12}\text{O}_{17}\text{Cl}_2$ (S7).

with mesoporous structures that allow for more efficient transport of the reactants to access the active sites. Consequently, the photocatalytic efficiency of the sample is enhanced [55]. Moreover, the good photocatalytic efficiency may be partially due to the flower-like micro/nano structures of the as-synthesized $\text{Bi}_{12}\text{O}_{17}\text{Cl}_2/\beta\text{-Bi}_2\text{O}_3$. Such three-dimensional interconnected channels made by nanosheets offer high surface-to-volume ratios and produce efficient transport pathways for the pollutants and their oxidation products during photocatalytic reactions [56], which can improve the mineralization efficiency of the system.

To elucidate the roles of the active oxygen species during the degradation of PTPB on the $\text{Bi}_{12}\text{O}_{17}\text{Cl}_2/\beta\text{-Bi}_2\text{O}_3$ composite (sample S4), free radicals trapping experiments were carried out by adding various scavengers. Isopropanol was used to scavenge $\cdot\text{OH}$, sodium oxalate was used to scavenge photogenerated h^+ , potassium dichromate was used to scavenge photogenerated e^- ,

4-hydroxy-2,2,6,6-tetramethylpiperidinyloxy (TEMPOL) was used to scavenge $\cdot\text{O}_2^-$, and N_2 was used to remove oxygen that was dissolved in the solution [57]. As shown in Fig. 11A, after adding isopropanol, the photodegradation efficiency remained almost unchanged as no scavenger was added. However, a noticeable inhibition in the photocatalytic degradation was observed in the presence of potassium dichromate, TEMPOL, sodium oxalate, or N_2 , suggesting the significance of $\cdot\text{O}_2^-$ and h^+ in this photo-oxidation process. This possibility may be further confirmed by using the EPR method (Fig. 11B), which reveals strong DMPO- $\cdot\text{O}_2^-$ -adduct signals after light irradiation. Therefore, the photocatalytic degradation of PTPB over the $\text{Bi}_{12}\text{O}_{17}\text{Cl}_2/\beta\text{-Bi}_2\text{O}_3$ photocatalyst under visible light irradiation may be dominated by $\cdot\text{O}_2^-$ radical (formed by the reaction of photogenerated electrons with dissolved oxygen) and directed hole oxidation instead of by $\cdot\text{OH}$ oxidation, which may explain the high mineralization of PTPB in the system.

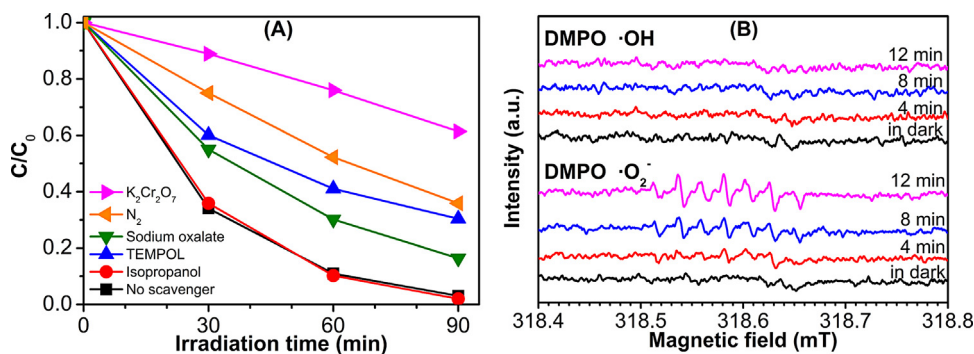


Fig. 11. (A) Photodegradation of PTPB over the as-synthesized $\text{Bi}_{12}\text{O}_{17}\text{Cl}_2/\beta\text{-Bi}_2\text{O}_3$ heterojunction (sample S4) in the presence of different scavengers: No scavenger, isopropanol, 4-hydroxy-2,2,6,6-tetramethylpiperidinyloxy (TEMPOL), sodium oxalate, N_2 , and potassium dichromate; (B) DMPO spin-trapping EPR spectra for DMPO- $\cdot\text{OH}$ and DMPO- $\cdot\text{O}_2^-$ under visible light irradiation with sample S4.

4. Conclusion

In summary, flower-like $\text{Bi}_{12}\text{O}_{17}\text{Cl}_2/\beta\text{-Bi}_2\text{O}_3$ composites with large contact interfaces were successfully synthesized using a facile solvothermal-calcining route. The ratio of $\text{Bi}_{12}\text{O}_{17}\text{Cl}_2$ to $\beta\text{-Bi}_2\text{O}_3$ is easily controlled by adding low concentrations of Cl^- . The formation of the $\text{Bi}_{12}\text{O}_{17}\text{Cl}_2/\beta\text{-Bi}_2\text{O}_3$ heterojunction plays key role in their superior visible light photocatalytic performances during the degradation of PTBP under visible light irradiation. The superoxide radicals and photogenerated holes were main reactive species for the photocatalytic degradation and mineralization of PTBP. The $\text{Bi}_{12}\text{O}_{17}\text{Cl}_2/\beta\text{-Bi}_2\text{O}_3$ heterojunction synthesized using this simple method may be applied to water purification and used in photo-voltaic cells, photonic and optoelectronic devices, sensors, and so on.

Acknowledgements

This work was financially supported by the National Natural Science Foundation of China (No. 21477040), the Natural Science Foundation of Guangdong Province of China (No. S2012040007074), and the Scientific Research Foundation of Graduate School of South China Normal University (No. 2013kyjj050 and No. 2014ssxm29).

Appendix A. Supplementary data

Supplementary data associated with this article can be found, in the online version, at <http://dx.doi.org/10.1016/j.apcatb.2015.01.015>.

References

- [1] D.W. Kolpin, E.T. Furlong, M.T. Meyer, E.M. Thurman, S.D. Zaugg, L.B. Barber, H.T. Buxton, *Environ. Sci. Technol.* 36 (2002) 1202–1211.
- [2] H.M. Kuch, K. Ballschmitter, *Environ. Sci. Technol.* 35 (2001) 3201–3206.
- [3] J.A. McLachlan, *Endocr. Rev.* 22 (2001) 319–341.
- [4] J.T. Yu, E.J. Bouwer, M. Coelhan, *Agr. Water Manage.* 86 (2006) 72–80.
- [5] H. Sun, X. Xu, J. Qu, X. Hong, Y. Wang, L. Xu, X. Wang, *Chemosphere* 71 (2008) 582–588.
- [6] U.I. Gaya, A.H. Abdullah, *J. Photoch. Photobio. C* 9 (2008) 1–12.
- [7] D. Chatterjee, S. Dasgupta, *J. Photoch. Photobio. C* 6 (2005) 186–205.
- [8] L. Huang, G. Li, T. Yan, J. Zheng, L. Li, *New J. Chem.* 35 (2011) 197–203.
- [9] R. He, S. Cao, P. Zhou, J. Yu, *Chin. J. Catal.* 35 (2014) 989–1007.
- [10] P. Madhusudan, J. Ran, J. Zhang, J. Yu, G. Liu, *Appl. Catal. B: Environ.* 110 (2011) 286–295.
- [11] N. Tian, H. Huang, Y. Guo, Y. He, Y. Zhang, *Appl. Surf. Sci.* 322 (2014) 249–254.
- [12] K. Brezesinski, R. Ostermann, P. Hartmann, J. Perlich, T. Brezesinski, *Chem. Mater.* 22 (2010) 3079–3085.
- [13] X. Xiao, W.D. Zhang, *J. Mater. Chem.* 20 (2010) 5866–5870.
- [14] W.L. Huang, Q.S. Zhu, *J. Comput. Chem.* 30 (2009) 183–190.
- [15] X. Xiao, C. Liu, R. Hu, X. Zuo, J. Nan, L. Li, L. Wang, *J. Mater. Chem.* 22 (2012) 22840–22843.
- [16] G. Chen, G.L. Fang, G.D. Tang, *Mater. Res. Bull.* 48 (2013) 1256–1261.
- [17] X. Lin, T. Huang, F. Huang, W. Wang, J. Shi, *J. Phys. Chem. B* 110 (2006) 24629–24634.
- [18] X. Xiao, J. Jiang, L. Zhang, *Appl. Catal. B: Environ.* 142–143 (2013) 487–493.
- [19] X. Xiao, C. Xing, G. He, X. Zuo, J. Nan, L. Wang, *Appl. Catal. B: Environ.* 148–149 (2014) 154–163.
- [20] Y. Tian, B. Chang, J. Lu, J. Fu, F. Xi, X. Dong, *ACS Appl. Mater. Interfaces* 5 (2013) 7079–7085.
- [21] Y. Huo, X. Chen, J. Zhang, G. Pan, J. Jia, H. Li, *Appl. Catal. B: Environ.* 148–149 (2014) 550–556.
- [22] M. Guan, D. Ma, S. Hu, Y. Chen, S. Huang, *Inorg. Chem.* 50 (2011) 800–805.
- [23] Y. Peng, M. Yan, Q. Chen, C. Fan, H. Zhou, A. Xu, *J. Mater. Chem. A* 2 (2014) 8517–8524.
- [24] Y. Xu, Z. Zhang, W. Zhang, *Mater. Res. Bull.* 48 (2013) 1420–1427.
- [25] A. Ren, C. Liu, Y. Hong, W. Shi, S. Lin, P. Li, *Chem. Eng. J.* 258 (2014) 301–308.
- [26] A. Hameed, M. Aslam, I.M.I. Ismail, N. Salah, P. Fornasiero, *Appl. Catal. B: Environ.* 163 (2015) 444–451.
- [27] L. Zhang, W. Wang, L. Zhou, M. Shang, S. Sun, *Appl. Catal. B: Environ.* 90 (2009) 458–462.
- [28] J. Fu, Y. Tian, B. Chang, F. Xi, X. Dong, *J. Mater. Chem.* 22 (2012) 21159–21166.
- [29] X. Zhang, L. Zhang, T. Xie, D. Wang, *J. Phys. Chem. C* 113 (2009) 7371–7378.
- [30] X. Xiao, R. Hao, M. Liang, X. Zuo, J. Nan, L. Li, W. Zhang, *J. Hazard. Mater.* 233 (2012) 122–130.
- [31] S.Y. Chai, Y.J. Kim, M.H. Jung, A.K. Chakraborty, D. Jung, W.I. Lee, *J. Catal.* 262 (2009) 144–149.
- [32] Y. Li, J. Wang, H. Yao, L. Dang, Z. Li, *Catal. Commun.* 12 (2011) 660–664.
- [33] G. Yang, Z. Jiang, H. Shi, T. Xiao, Z. Yan, *J. Mater. Chem.* 20 (2010) 5301–5309.
- [34] X. Xiao, R. Hu, C. Liu, C. Xing, C. Qian, X. Zuo, J. Nan, L. Wang, *Appl. Catal. B: Environ.* 140–141 (2013) 433–443.
- [35] J. Cao, B. Luo, H. Lin, B. Xu, S. Chen, *Appl. Catal. B: Environ.* 111 (2012) 288–296.
- [36] F. Li, Q. Wang, X. Wang, B. Li, Y. Hao, R. Liu, D. Zhao, *Appl. Catal. B: Environ.* 150–151 (2014) 574–584.
- [37] L. Shen, N. Bao, Y. Zheng, A. Gupta, T. An, K. Yanagisawa, *J. Phys. Chem. C* 112 (2008) 8809–8818.
- [38] J.M. Song, C.J. Mao, H.L. Niu, Y.H. Shen, S.Y. Zhang, *CrystEngComm* 12 (2010) 3875–3881.
- [39] Z. Zhao, F. Liu, L. Zhao, S. Yan, *Appl. Phys. A* 103 (2011) 1059–1065.
- [40] F. Peng, C. Chen, H. Yu, H. Wang, J. Yang, *Mater. Chem. Phys.* 116 (2009) 294–299.
- [41] X. Wang, Q. Wang, F. Li, W. Yang, Y. Zhao, Y. Hao, S. Liu, *Chem. Eng. J.* 234 (2013) 361–371.
- [42] M.N. Gómez-Cerezo, M.J. Muñoz-Batista, D. Tudela, M. Fernández-García, A. Kubacka, *Appl. Catal. B: Environ.* 156–157 (2014) 307–313.
- [43] M. Schmidt, H. Oppermann, M. Binnewies, Z. Anorg. Allg. Chem. 625 (1999) 1001–1012.
- [44] H. Kodama, S. Horiuchi, A. Watanabe, *J. Solid State Chem.* 75 (1988) 279–284.
- [45] J.H. Yao, K.R. Elder, H. Guo, M. Grant, *Phys. Rev. B* 45 (1992) 8173–8176.
- [46] Y. Qiu, M. Yang, H. Fan, Y. Zuo, Y. Shao, Y. Xu, X. Yang, S. Yang, *Cryst. Eng. Comm.* 13 (2011) 1843–1850.
- [47] H. Cheng, B. Huang, J. Lu, Z. Wang, B. Xu, X. Qin, X. Zhang, Y. Dai, *Phys. Chem. Chem. Phys.* 12 (2010) 15468–15475.
- [48] K. Sing, D.H. Everett, R. Haul, L. Moscou, R.A. Pierotti, J. Rouquerol, T. Siemieniowska, *Pure Appl. Chem.* 57 (1985) 603–619.
- [49] J. Xu, W. Meng, Y. Zhang, L. Li, C. Guo, *Appl. Catal. B: Environ.* 107 (2011) 355–362.
- [50] Y. Wang, Y. Wen, H. Ding, Y. Shan, *J. Mater. Sci.* 45 (2010) 1385–1392.
- [51] M.A. Gondal, X.F. Chang, Z.H. Yamani, *Chem. Eng. J.* 165 (2010) 250–257.
- [52] L. Ge, C. Han, J. Liu, *Appl. Catal. B: Environ.* 108 (2011) 100–107.
- [53] J. Hou, C. Yang, Z. Wang, W. Zhou, S. Jiao, H. Zhu, *Appl. Catal. B: Environ.* 142 (2013) 504–511.
- [54] F. Dong, Z. Zhao, T. Xiong, Z. Ni, W. Zhang, Y. Sun, W. Ho, *ACS Appl. Mater. Interfaces* 5 (2013) 11392–11401.
- [55] J. Zhang, F. Shi, J. Lin, D. Chen, J. Gao, Z. Huang, X. Ding, C. Tang, *Chem. Mater.* 20 (2008) 2937–2941.
- [56] A.T. Bell, *Science* 299 (2003) 1688–1691.
- [57] W. Wang, Y. Yu, T. An, G. Li, H.Y. Yip, J.C. Yu, P.K. Wong, *Environ. Sci. Technol.* 46 (2012) 4599–4606.